A methodology for boundary condition optimization in 3D-CFD of internal combustion engines

Applied Thermal Engineering 292 (2026) 130270

Contents lists available at ScienceDirect

Applied Thermal Engineering

journal homepage: www.elsevier.com/locate/ate

Research Paper

A methodology for boundary condition optimization in 3D-CFD of internal combustion engines

Simona Gurrì [a], Oscar Vento [a,*], Omar Marello [a], Roberto Finesso [a], Alessandro Gallo [b], Luca Vargiu [b], Alessandro Ferrari [a]

[a] DENERG - Energy Dept., Politecnico di Torino, Corso Duca degli Abruzzi, Turin, 10129, Italy
[b] FPT, via Puglia 15, Turin, 10156, Italy

ARTICLE INFO

Keywords:
3D computational fluid dynamics
Internal combustion engines
Boundary condition
Heat transfer
Wall temperatures

ABSTRACT

This study presents a novel computationally efficient methodology for tuning boundary conditions in 3D CFD simulations of internal combustion engines. The objective is to achieve errors below 1% for in-cylinder pressure at spark timing and below 5% for intake mass. The approach employs an iterative procedure which is grounded on thermodynamic principles, applying the laws of thermodynamics based on both numerical and experimental data during the compression phase. A multi-zone convection model is developed to optimize wall temperatures, while intake pressure is adjusted using physics-informed considerations. In order to refine the multi-zone heat transfer coefficients, the method incorporates a hybrid optimization approach that combines simulated annealing with interior point methods. The methodology is tested on a heavy-duty port fuel injection spark-ignition engine fueled by compressed natural gas. The results demonstrate the effectiveness of this methodology in improving the accuracy of CFD simulations for internal combustion engines, providing a robust framework for boundary condition optimization. This allows the number of 3D simulations required for model tuning and calibration to be reduced compared to trial-and-error or DoE approaches, enhancing model predictive capability.

1. Introduction

The need for decarbonization and the reduction of pollutant emissions in the mobility sector still requires significant research efforts. Although powertrain electrification plays an increasingly important role in achieving this goal, the internal combustion engine (ICE) cannot be easily replaced in several applications, such as heavy-duty long-haul transport and the waterborne sector [1]. The limitations for the adoption of battery-electric powertrain solutions in these cases are numerous: for example, battery electric vehicles can achieve driving ranges of the order of only 300–500 km [2], while, the economic competitiveness for electric ships is only observed for distances of up to 2500 km [3]. A second issue is related to the high battery weight, which could significantly reduce the available payload up to 25% in long-haul transport; moreover, batteries still require considerably long charging times [2] and remain very expensive compared to ICE-based solutions [4]. Finally, it is worth pointing out that the environmental impact of fully electric powertrains is largely dependent on the energy mix used for power generation [5]. Therefore, ICE technology will continue to play a significant role in the coming decades and research efforts will continue to be conducted to limit its environmental impact, including hardware optimization and the use of alternative fuels, such as low-carbon options (e.g. hydrogen and ammonia [6]), e-fuels and biofuels of second generation [1]. Numerical simulation can provide a significant contribution in reducing the required experimental efforts and costs, as well as in supporting experiments with physical explanations. In particular, 3D Computational Fluid Dynamics (CFD) models have the potential of accurately reproducing the complex local phenomena which occur inside the combustion chamber, including the fuel spray characteristics, the air–fuel mixture formation, the fuel oxidation and the pollutant emission formation. However, they suffer several limitations, such as the high required computational resources, the long simulation times, the sensitivity to the mesh quality and to the boundary and initial conditions.

Computational resources are growing in power and accessibility, making it possible on the one hand, to perform increasingly accurate simulations with finer grids and, on the other hand, to develop models validated over a wider range of conditions than in the past, or to consider a greater number of case studies. However, non-optimal boundary conditions (BCs) may significantly affect the quality of the results since numerical models based on Navier–Stokes partial differential equations

* Corresponding author.
E-mail address: oscar.vento@polito.it (O. Vento).

https://doi.org/10.1016/j.applthermaleng.2026.130270
Received 15 December 2025; Received in revised form 28 January 2026; Accepted 12 February 2026
Available online 13 February 2026

Nomenclature

Symbols and acronyms

α	Temperature scaling factor
χ	Coefficient for pegging
γ	Cooling rate of simulated annealing optimization
Δ	Pressure pegging value
δ	Pressure drop across intake valves
ΔE	Difference between candidate and current solution of the objective function
ϵ	Turbulent dissipation
λ	Regularization parameter of objective function
A_i	Surface area of the i^{th} boundary
AMR	Adaptive Mesh Refinement
aTDCf	After Top Dead Center Firing
BCs	Boundary Conditions
BDC	Bottom Dead Center
CFD	Computational Fluid Dynamics
CHT	Conjugate Heat Transfer
CI	Compression Ignition
CNG	Compressed Natural Gas
c_p	Specific heat at constant pressure
c_v	Specific heat at constant volume
$E_{\%}$	Relative percentage error
DoE	Design of Experiments
FEA	Finite Element Analysis
$f(h_i)$	Objective function
HD	Heavy Duty
$\tilde{h}_i$	3-D heat transfer coefficient for the i^{th} boundary
h_i	Quasi-D heat transfer coefficient of the i^{th} boundary
ICE	Internal Combustion Engine
k	Turbulent kinetic energy
L_w	Viscous Dissipation
m	Mass
p	Pressure
P_{accept}	Acceptance probability function
PFI	Port Fuel Injection
Q	Heat transfer
$\dot{Q}$	Heat flux
R	Gas constant
RANS	Reynolds-averaged Navier–Stokes equations
S	Entropy
SI	Spark ignition
T	Temperature
t	Time in engine crank-angles
V	Volume

Subscripts

BC	Referring to boundary condition
$bound$	Referring to boundaries
IM	Referred to intake manifold
IVC	Intake Valve Closure
SA	Spark Advance
abs	Absolute
exp	Experimental
i	Referring to the i^{th} boundary
int	Referring to intake
new	Referring to new value
num	Numerical
nw	Referring to proximity of the wall
old	Referring to old value
$pred$	Referring to predicted values of the interior point optimization method
rel	Relative
$wall$	Referring to the combustion chamber walls

Superscripts

0	Referring to initial values of simulated annealing optimization
$current$	Referring to current value of simulated annealing optimization
new	Referring to candidate solution of simulated annealing
opt	Referring to simulated annealing optimization

are sensitive to these input data. For example, the study reported in [7] shows how the imposed head wall temperature has a significant impact on the predicted heat flux in ICEs, which in turn can affect other related quantities, such as inducted charge mass and heat release. Wall temperatures cannot be easily measured experimentally [8], as this requires expensive techniques such as drilling operations to install thermocouples, or optical techniques [9]. Therefore, wall temperatures are typically evaluated on the basis of preliminary 1D simulations [10], of specific engine thermal models [11], such as those presented in [12], or are simply assumed. A review of wall temperature estimation methods is reported in [8]. As an alternative to the law-of-the-wall usage for the wall heat transfer simulation, two numerical approaches have been developed: the Finite Element Analysis (FEA) for solid parts and the CFD-CHT (Conjugate heat transfer) method, where imposed wall temperatures are used only as initial values and they are automatically updated during the simulation, computing the heat transfer from the fluid to the walls, considering the thermal properties of the material of which they are made. This leads to a natural evolution of the temperature field, reflecting the actual interaction between fluid and solid. When the FEA approach is adopted, the fluid domain and the solid one are solved separately: the former with the CFD tool, the latter with a finite element technique for heat conduction in solids [13]. As an example, a CFD-FEA technique has been used to analyze the effect on the heat transfer of a thermal barrier coating applied to the piston of either a diesel [14] or a spark ignition (SI) engine [15] engine. The CFD-CHT approach, where the thermal interaction between the solid body and the fluid is simultaneously solved with the fluid governing equations, has been applied in different ICE test cases [16–18]: for example, a CFD–CHT simulation using the Buckingham Pi-Theorem is presented in [19] to analyze heat transfer in a turbocharged SI engine: effects of ignition timing, air–fuel ratio, and boost pressure effects on component temperatures are examined. As can be easily understood, the usage of both CFD-FEA and CFD-CHT techniques dramatically increases the computational time.

Furthermore, it is important to note that uncertainty in the boundary conditions may require performing several simulations for optimal tuning, for example, by adopting DoE approaches, which would consequently increase computational time. In addition to computational resources and reliable boundary conditions, accurate experimental data are needed for 3D-CFD models validation, which is not always achievable due to high instrumentation costs or measuring device characteristics. For example, in-cylinder pressure is typically measured using

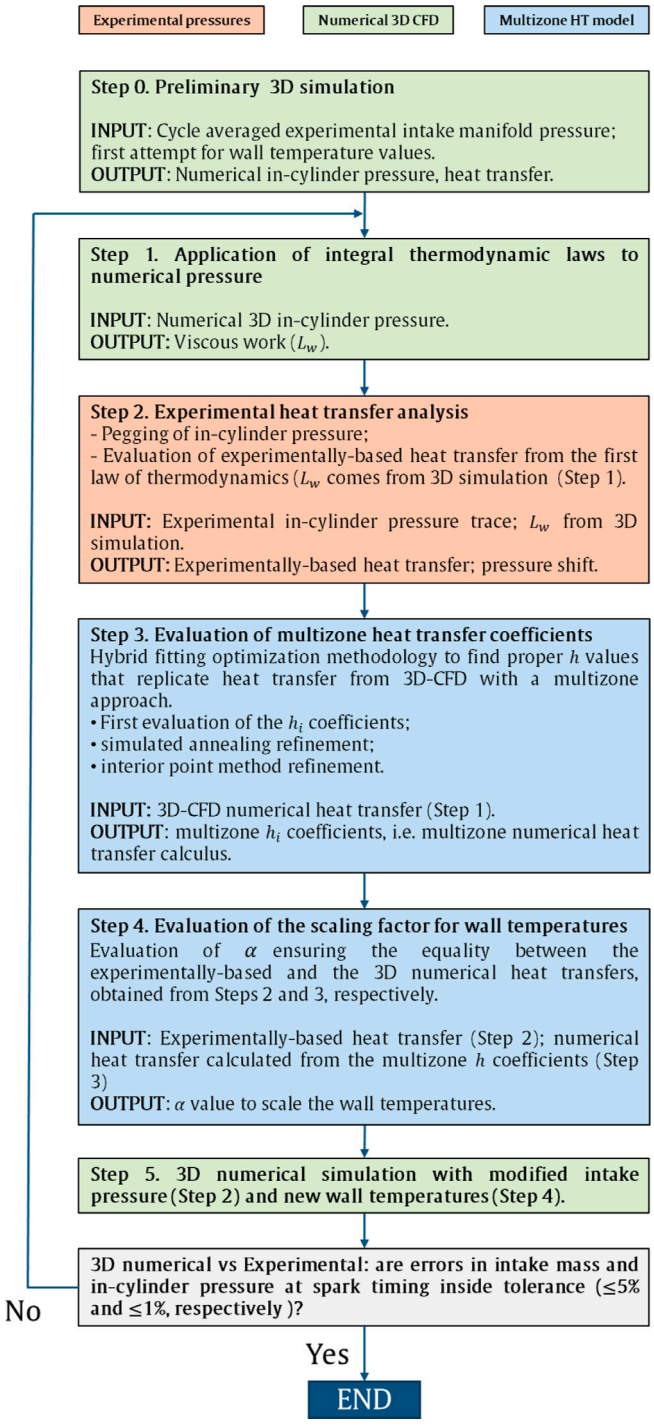

Fig. 1. Methodology flow-chart.

piezoelectric transducers that provide a relative measure [20]. Therefore, the acquired in-cylinder pressure needs to be adjusted in order to estimate its absolute value [21], and this is typically done by imposing that the pressure around the bottom dead center (BDC) of the intake stroke is equal to the intake manifold pressure. Nevertheless, even this procedure introduces a certain degree of uncertainty.

The scope of this work is filling a gap in the literature on a systematic and rapid procedure to adjust boundary condition in 3D-CFD simulations of internal combustion engines. Specifically, the present study introduces a novel methodology for boundary condition optimization in 3D-CFD engine models, addressing the limitations of existing approaches, and significantly reducing both computational time and instrumentation costs. The proposed procedure is predictable, reproducible, and independent of user experience, eliminating the need for trial-and-error tuning. In particular, by leveraging thermodynamic principles and employing a dual-step optimization strategy, the method enables iterative adjustment of the boundary wall temperatures, in-cylinder experimental pressure and intake pressure, so as to obtain an accurate estimation of the in-cylinder pressure trace before combustion and trapped charge mass. The approach achieves high accuracy, with errors in pressure at spark timing below 1%, and intake mass prediction errors remaining under 5% with a small number of 3D simulations, especially when compared to trial-and-error or design of experiments (DoE) approaches. Ensuring accurate conditions at combustion onset is essential to develop reliable and predictive 3D-CFD models. The approach offers a computationally efficient alternative to more resource-intensive calibration approaches while maintaining high accuracy, representing a novel contribution to the field of engine simulation.

The structure of the paper is described below. In Section 2, the iterative process for the minimization of errors in some boundary conditions and input data is thoroughly described. In Section 3, a case study is presented to validate the model that implements the innovative procedure, and the results are described and discussed. Finally, in Section 4, conclusions are drawn on the methodology effectiveness.

2. Methodology

The goal is to set the intake pressure and wall temperature boundary conditions in the 3D-CFD model so that the resulting intake mass and pressure at spark timing closely match the experimental data with errors below 5% and 1% respectively, which represent the convergence criteria of the iterative procedure. The methodology is here described in detail. A complete overview of the process is illustrated in Fig. 1, which represents each stage of the methodology with color-coded blocks indicating the type of data under consideration: experimental pressure data in orange, 3D numerical simulation in green and multi-zone heat transfer modeling in light blue.

The process begins (Step 0) with a preliminary 3D simulation using the measured value of the average intake manifold pressure and a set of wall temperature values, for example derived from the literature, experience or from a 1D engine model. The primary outputs of interest for this simulation include in-cylinder pressure and heat transfer throughout the compression phase. In Step 1 (described in Section 2.1), the laws of thermodynamics are applied to the numerical results obtained in Step 0, with the objective of estimating the viscous friction work L_w. In Step 2, the experimental in-cylinder pressure trace is considered and adjusted to compensate for potential referencing errors as described in Section 2.2. The outcome of this step is a properly referenced experimental pressure curve, taking into account pressure drops through the valves and intake system based on the 3D preliminary simulation, and possible measuring inaccuracies. Subsequently, the integral laws of thermodynamics are applied to compute the heat transfer calculated with the corrected in-cylinder experimental pressure and referred to as "experimentally-based" heat transfer. Once the 3D-CFD and the experimentally-based heat transfer curves are compared, the primary objective is to make the numerical heat transfer virtually equal to the experimentally-based one, adjusting the wall temperatures. To this purpose, in Step 3 (described in Section 2.3), a multi-zone heat transfer model is developed with the aim of replicating the heat transfer results of the 3D model run in Step 0. This is done by tuning the heat transfer coefficients h of every wall through a dual-step fitting optimization process, as described in detail in Section 2.3. At the end of Step 4, the resulting multi-zone heat transfer model is able to reproduce the heat transfer of the 3D-CFD one. Once the multi-zone heat transfer model is established, it is used in Step 4 (described in Section 2.4) to determine the appropriate wall temperature of each boundary that

allows the global experimentally-based heat transfer obtained at Step 3 to be matched. Specifically, this is done by evaluating a scaling factor (α), which acts as a multiplier for all the boundary wall temperatures by maintaining their initial relative ratio.

In Step 5 (described in Section 2.5), once α has been determined, it is directly applied to set up the wall temperature boundary conditions of a new 3D numerical simulation, together with a modified intake pressure boundary condition, which takes into account the shift applied in Step 2 to the experimental in-cylinder pressure. If the results of the new 3D simulation in terms of pressure at spark timing and intake mass show good agreement with experimental data (errors below 1% and 5%, respectively are accepted), the selected wall temperature values are considered correct and the procedure can be ended.

Instead, if discrepancies persist in the pressure at spark ignition or in the intake mass, this indicates that the heat transfer is not yet accurate and, therefore, the procedure must restart from Step 1. For all the considered cases, this iterative refinement converged to a satisfactory solution within one to three iterations.

2.1. Application of the laws of thermodynamics to numerical pressure

After the preliminary 3D simulation (Step 0 in Fig. 1), the fundamental thermodynamic relation is applied, using the numerical results, to the mass inside the cylinder, following a Lagrangian approach from the intake valve closure (IVC) to the spark advance (SA), as follows in Eq. (1):

$$\int_{IVC}^{SA} T\,dS = \int_{IVC}^{SA} p dV + \int_{IVC}^{SA} c_v m dT \tag{1}$$

where T stands for the temperature, S for the entropy, p for the pressure, V represents the cylinder volume, c_v the specific heat at constant volume, and m is the trapped mass inside the cylinder at the end of the intake phase. Eq. (1) allows to estimate the entropy-related integral to be estimated, since pressure and temperature fields are known from the simulation, and V comes from engine geometrical data. Subsequently, the following relation is considered:

$$\int_{IVC}^{SA} T\,dS = Q + L_w \tag{2}$$

where Q is the 3D-CFD model output representing the heat transfer through the combustion chamber surfaces and L_w indicates the viscous dissipation. The latter quantity can therefore be determined based on Eq. (2) since Q is known and the entropy-related integral can be computed from Eq. (1).

2.2. Experimentally-based heat transfer

The heat transfer through the walls is subsequently calculated using the measured values of in-cylinder pressure, mass and temperature (denoted with the "exp" subscript), under the hypothesis of quasi-perfect gas ($c_v = c_v(T)$, $c_p = c_p(T)$ and $c_p(T) - c_v(T) = R = const$), using the following relation, derived by combining Eqs. (1) and (2):

$$Q_{exp} = \int_{IVC}^{SA} p_{exp} dV + \int_{IVC}^{SA} c_v m_{exp} dT_{exp} - L_w \tag{3}$$

where T_{exp} can be computed on the basis of the perfect gas law ($p_{exp}V = m_{exp}RT_{exp}$). The mass m_{exp} is given by the sum of the measured inflow mass and the numerical dead-volume mass at the beginning of the intake stroke (the latter mass cannot be experimentally measured). The value of the viscous dissipation L_w used in Eq. (3) is determined from the numerical data in Section 2.1, since it cannot be estimated experimentally. Furthermore, the measured pressure signal p_{exp} used in the equation is the average of all the cycles acquired for all the cylinders, one-by-one preliminary filtered with a low-pass filter to remove non-physical higher-order harmonics and then pegged to the measured absolute pressure in the intake manifold (p_{IM}) starting from the relative in-cylinder pressure $p_{exp,rel}$:

$$p_{exp} = p_{exp,rel} + p_{IM} \tag{4}$$

where $p_{exp,rel}$ at BDC is 0 Pa. The obtained heat transfer curve is highly dependent on the pressure curve, since the $\int p_{exp} dV$ term is predominant in Eq. (3) during the compression process. In principle, the experimentally-based heat transfer curve may differ in shape from the numerical heat transfer. This may be due to inaccuracies in the 3D-CFD model, but also to errors in the pegging procedure of the experimental pressure. In fact, this procedure sets the average in-cylinder pressure around BDC of the intake stroke equal to the intake manifold pressure, thus neglecting, for example, any pressure drop through the intake valves. It was verified that a pressure adjustment of a few millibars can affect the obtained Q_{exp} to a great extend (this will be shown in Section 3). Therefore, a new method has been introduced to refine the pegging of the experimental pressure traces. First, difference δ between the intake manifold pressure (set as intake pressure boundary condition at Step 0) and the space-averaged pressure at the BDC in the combustion chamber obtained as an output of the 3D-CFD model of Step 0 is calculated. This difference is used to downward shift the whole experimental pressure curves by means of the following equation:

$$p_{exp} = p_{exp,rel} + p_{IM} - \chi \cdot \delta = p_{exp,rel} + p_{IM} - \Delta \tag{5}$$

where χ is a correction coefficient that multiplies δ ($\Delta := \chi \cdot \delta$) compensating for possible errors in the model (c.f. next subsection).

2.3. Evaluation of the multi-zone heat transfer coefficients

Given a chosen value of Δ, in order to evaluate the wall temperature scaling factor α, a multi-zone approach is applied to compare the 3D numerical heat transfer with the experimentally-based one. It is worth noting that the heat transfer through the wall is mainly due to convection for a SI engine, while radiation provides a negligible contribution [22]. Hence, it is possible to write the following relation, which sets the experimentally based value of the cumulative heat transfer Q_{exp} to be equal to the numerical one Q_{num}:

$$\begin{aligned} Q_{exp}(t) &= \sum_{i=1}^{n} \int_{IVC}^{SA} \dot{Q}_{i,num}(t) dt = Q_{num} \\ &= \sum_{i=1}^{n} \int_{IVC}^{SA} h_i(t) A_i(t) [T_{mean}(t) - \alpha T_{wall,i}] dt \end{aligned} \tag{6}$$

where t is the time expressed as a function of engine crank-angles and engine angular speed from intake valve closure (IVC) to spark timing (SA). In Eq. (6) the numerical cumulative heat transfer has been expressed as a summation over the $n = 6$ boundaries (i.e., walls) of the combustion chamber which are shown in Fig. 2 (multi-zone approach). In particular, in Eq. (6) A_i is the surface of each boundary of the combustion chamber (cf. Fig. 2); T_{mean} is the space-averaged temperature of the charge in the combustion chamber (this is a result of the numerical simulation) and h_i is the multi-zone convection coefficient for the i^{th} boundary. The approach is referred to as multi-zone because, although the convective heat transfer formula exploits the mean temperature inside the chamber, accounting for the cross-coupling between boundaries of in-cylinder thermodynamics, it considers all the different wall temperatures $T_{wall,i}$ for the n boundaries in the combustion chamber depicted in Fig. 2. The multi-zone heat transfer coefficients have to be computed based on the 3D-numerical results. In fact, each h_i is an equivalent convective heat-transfer coefficient for boundary i, which allows the same heat transfer through that boundary as in the 3D CFD model, using the mean gas temperature in the combustion chamber.

It should be noted that the multi-zone h_i coefficients of Eq. (6) differ from the heat transfer coefficients $\tilde{h}_i$, defined in the 3D numerical model to satisfy the following equation, in which the heat transfer is

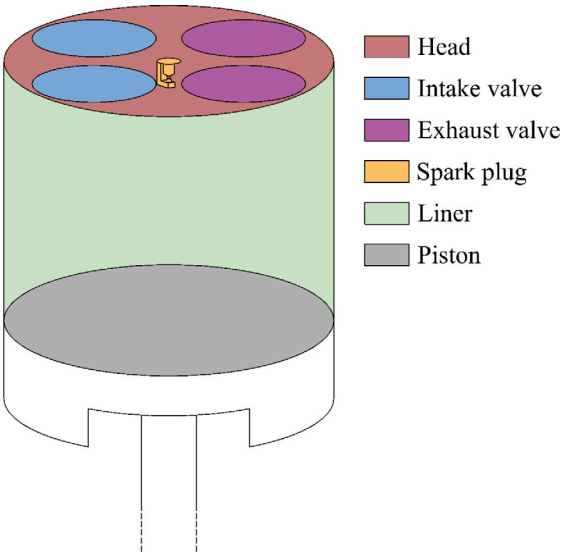

Fig. 2. Walls and boundaries of the numerical model.

expressed as a function of the temperature of the cells in the proximity of the wall ($T_{num,nw}$):

$$Q_{num}(t) = \int_{IVC}^{SA} \dot{Q} dt = \\ = \int_{IVC}^{SA} \left(\int_{A} \tilde{h}_i A_i [T_{num,nw} - T_{wall,i}] dA \right) dt \tag{7}$$

Temperature $T_{num,nw}$ is intrinsically three-dimensional, differing from the space-averaged temperature T_{mean}, and as a result, for each boundary, $\tilde{h}_i$ in Eq. (7) differs from h_i in Eq. (6). Hence, a single convective heat transfer coefficient is determined for each boundary and only the space-averaged instantaneous combustion chamber value for the fluid temperature, T_{mean}, is necessary. Although using the average temperature near each wall along with its average heat transfer coefficient is a viable approach in the framework of this methodology (both are output data of the 3D CFD simulation), reducing the problem complexity by exclusively using T_{mean} has been demonstrated to facilitate more rapid convergence to the optimal set of boundary conditions, as will be clarified in sub Section 2.4.

While numerous 0D models for heat transfer in internal combustion engines are available in the literature [23,24], which assume a unique wall temperature, the proposed multi-zone approach can account for the contribution of each boundary wall to the overall heat transfer process during the compression phase.

2.3.1. The heat transfer coefficient optimization procedure

It requires to identify the optimal values of the h_i heat transfer coefficients that accurately replicate the numerical heat transfer of the 3D-CFD model while ensuring physical feasibility and computational efficiency.

To this aim, a hybrid strategy has been developed, consisting of three main steps:

1. setting initial approximate values for the multi-zone heat transfer coefficients (one coefficient for each i^{th} boundary);
2. global search optimization using the simulated annealing algorithm;
3. local search optimization using the interior point method;

The first-attempt value of the multi-zone heat transfer coefficients, namely h_i^*, are obtained by imposing that, at each time, the 3D numerical heat flux across each boundary is defined by the following formula:

$$h_i^*(t) = \frac{\dot{Q}_{num,i}}{A_i \Delta T_{bound,i}} \qquad \forall\ i = 1, 2, \dots, n \tag{8}$$

where $\dot{Q}_{num,i}$ is the heat flux obtained from the 3D numerical model for the i^{th} of the n boundaries currently under analysis and $\Delta T_{bound,i} := T_{mean,num}(t) - T_{wall,i}$. The heat transfer coefficient of each boundary is optimized separately. The constraint of each optimization problem is that the contribution to the total heat transfer of that boundary must be equal to that resulting from the 3D-CFD simulation.

In what follows, the dependence of the heat transfer coefficients $h_i^*(t)$ and of the other variables from time t is always assumed, even if the notation omits the argument (t) for brevity.

Based on Eq. (8) h_i^* is infinite when $T_{mean,n}(t) = T_{wall,i}$, i.e., $\Delta T_{bound,i} = 0$. Consequently, the definition is applied for values of $|\Delta T_{bound,i}|$ sufficiently higher than zero in order to avoid the vicinity to the asymptote from both sides, where the function begin to diverge, reflecting a non-physical phenomena (for the considered case, $h_i^*(t)$ diverged for values lower than 10 to 50 K depending on the boundary). A polynomial regression is used to obtain a continuous function across the entire duration of the compression process. Due to the lack of definition of h_i^* when $|\Delta T_{bound,i}| < 10 \div 50$ K, the initial value obtained from Eq. (8) does not satisfy Eq. (6), i.e., it does not allow the cumulative experimental heat transfer to be equal to the numerical one.

A hybrid optimization approach has been implemented to refine the heat transfer coefficient, combining two optimization techniques: the simulated annealing algorithm and the interior point method. The objective function $f(h_i)$ in this optimization approach is designed to minimize the difference between the cumulative heat transfer determined with the multi-zone h_i coefficients and the cumulative heat transfer obtained as an output from the numerical model, while also ensuring smoothness of the solution. Such a function is defined as follows:

$$f(h_i) = \underbrace{\int_{IVC}^{SA} \left[(h_i A_i \Delta T_{bound,i}) - \dot{Q}_{num,i} \right]^2 dt}_{\text{Error term}} + \\ + \underbrace{\lambda \sum_{j=1}^{N-1} \left| \frac{\partial h_i}{\partial t} \right|_j}_{\text{Regularization term}} \tag{9}$$

where h_i is the heat transfer coefficient which satisfies the optimization process, $\lambda = 10^{-3}$ is the L1 norm regularization parameter that controls the trade-off between the fitting of the data and the smoothness of h_i over time and N is the number of timesteps between IVC and SA. The value of λ has been chosen using a stability-based criterion, in order to reduce spurious oscillations in the optimized $h_i(t)$.

In particular, it is possible to distinguish two contributions in Eq. (9), i.e., the error term and the regularization term. The error term calculates the squared difference between the heat flux predicted with the h_i coefficients and the reference heat flux of the numerical model, integrated over the simulation time. The regularization term promotes smoothness in the optimized heat transfer coefficients h_i as it penalizes sharp changes with respect to the crank angle variations in time; in fact, the absolute value of the partial derivative of h_i with respect to time is summed over all timesteps.

Simulated annealing. The simulated annealing algorithm [25], which is one of the most used metaheuristic optimization algorithms [26–29], is employed as the first step in the hybrid optimization approach, presented for the determination of the h_i values. Simulated annealing is useful for exploring the entire parameter space for heat transfer coefficients under optimization due to its stochastic search characteristics and its ability to escape from local optima. It is hence able to converge towards a global optimum. The algorithm operates as follows:

1. a random solution h_i^0 and an initial simulated annealing temperature $T_0^{opt} = 100$ are selected (the latter is a global optimization parameter that varies with iterations and is referred to as the "optimization temperature" to distinguish it from a physical one). h_i^0 values are obtained by adding a small random perturbation over the polynomial regression of h_i^*, given by Eq. (8);
2. a new candidate solution h_i^{new} is generated by applying a small random perturbation to the current solution (for the first iteration, $h_i^{new} = h_i^0$, while $h_i^{current} = h_i^*$);
3. the change in the objective function, $\Delta E = f(h_i^{new}) - f(h_i^{current})$ is calculated, where $f(h_i)$ is given by Eq. (9). One refers to ΔE as the energy variation between two states;
4. the acceptance probability function, namely P_{accept}, providing the probability to update the $h_i^{current}$, is computed as follows:

$$P_{accept} = \begin{cases} 1 & \text{if } \Delta E < 0 \\ e^{-\Delta E/T^{opt}} & \text{if } \Delta E \geq 0 \end{cases}$$

5. the temperature T^{opt} is decreased according to the parameter γ, referred to as the cooling schedule:

$$T_k^{opt} = T_0^{opt}\ \gamma^k$$

where $\gamma = 0.95$ is the selected cooling rate (typically $0.9 < \gamma < 0.99$, i.e., always monotonically decreasing optimization temperature).
6. steps 3–6 are repeated until a stopping criterion is met (in the present case, represented by the maximum number of iterations, which is set to 10^5).

In this implementation, simulated annealing algorithm is applied to each boundary separately, resulting in a runtime of approximately 3 min per boundary with an Intel Core i7-6700 CPU @3.4 GHz and 32 GB RAM. This stochastic global search enables the exploration of the parameter space comprehensively, mitigating the risk of being trapped in local optima. However, since simulated annealing is an unconstrained problem, there is no guarantee that the objective function tends to zero within the maximum number of iterations and, therefore, the error in the predicted heat transfer could be unacceptable; hence, the results of this global search are fed into the subsequent local optimization algorithm, which is the interior point method.

Interior point method. After the identification of a preliminary solution by means of the simulated annealing global search approach, the interior point method [30] is employed to improve the accuracy of the predicted heat transfer. This method is particularly effective for solving constrained optimization tasks. The problem is formulated as follows:

$$\min_{h_i} f(h_i) \quad \text{subject to} \quad Q_{pred,i} = Q_{num,i} \tag{10}$$

where $f(h_i)$ is the objective function as defined in Eq. (9) and $Q_{pred,i}$ is defined as follows:

$$Q_{pred,i}(h_i) \equiv \int_{IVC}^{SA} (h_i A_i \Delta T_{bound,i}) dt \qquad \forall\ i = 1, 2, \ldots, n \tag{11}$$

The equality in Eq. (10) represents the physical constraint on the heat transfer coefficients, i.e. the multi-zone and the 3D heat transfer through each boundary i must be the same, allowing to obtain the exact heat transfer when summed across the zones.

To solve this constrained problem, the interior point method systematically handles constraints by incorporating them into the objective function. This is done by introducing a loss function, which transforms the original problem into a series of unconstrained optimization problems. This function penalizes any deviation from the constraint, effectively guiding the solution as the optimization progresses.

The interior point method is applied to each boundary using the results from the simulated annealing method as the starting point. It takes approximately 10 min per boundary to fine-tune the heat transfer coefficients within the physically desirable region with an Intel Core i7-6700 CPU @3.4 GHz and 32 GB RAM. The combined use of the simulated annealing for initial exploration and of the interior point method for final refinement requires an overall reasonable computational time.

2.4. Evaluation of the scaling factor for wall temperatures

Once the h_i multi-zone heat transfer coefficients are found, wall temperatures scaling factor α can be computed from Eq. (6) so as to align the simulated heat transfer to the experimentally-based one.

$$\alpha = \frac{Q_{exp} - \sum_{i=1}^{n} \int_{IVC}^{SA} h_i A_i T_{mean} dt}{\sum_{i=1}^{n} \int_{IVC}^{SA} h_i A_i T_{wall,i} dt} \tag{12}$$

The wall temperature scaling factor determined using this approach proves more effective than the value obtained from the average near-wall temperatures ($T_{near,wall}$) and the related heat transfer coefficients derived directly from the 3D simulation results (cf. Eq. (7)). Notably, the latter method produces values that, being generally closer to unity if compared to those computed from Eq. (12) for the analyzed cases, leads to a substantially greater number of 3D CFD simulation runs.

2.5. 3D numerical simulation with modified intake pressure and new wall temperatures

The intake pressure is adjusted according to the chosen pegging value $\Delta = \chi \cdot \delta$. In fact, the experimental pressure in the combustion chamber is lower than the intake pressure by δ, which accounts for the pressure drop across the intake valves. The arbitrary coefficient χ is introduced to consider two sources of error: the first one is due to any possible inaccuracy in the measurement of the experimental intake manifold pressure, the second one is represented by the inaccuracy introduced in the numerical model by imposing a constant value of pressure in the intake manifold as a boundary condition, instead of a pressure time–history. It was verified that the intake valve pressure drop δ keeps almost constant from one iteration to the other of process in Fig. 1, since this pressure drop mainly depends on the engine speed. The intake manifold pressure boundary condition ($p_{BC,IM}$) is modified as follows:

$$p_{BC,IM,new} = p_{BC,IM,old} - [(\chi - 1) \cdot \delta] \tag{13}$$

while the wall temperature values imposed as boundary condition in the previous 3D numerical simulation are multiplied by the scaling factor α.

3. Methodology application and discussion

The developed approach for boundary condition optimization was applied to an FPT heavy-duty (HD) port fuel injection (PFI) SI engine fueled with compressed natural gas (CNG), which was simulated using a commercial CFD software. The engine represents a low pollutant emission redesign of a highly used heavy-duty diesel engine, leveraging the benefits of natural gas as a cleaner alternative to replace traditional diesel fuel in heavy-duty applications.

The geometrical characteristics of the engine are briefly summarized in Table 1, which provides key dimensions and specifications that define the engine architecture, while the 3D cylinder model used in the simulations is depicted in Fig. 3. This detailed surface captures the complex geometry of the combustion chamber, including piston bowl, cylinder head, valves, spark plug geometry, intake and exhaust ports.

Table 1
Engine geometry.

Turbocharged HD PFI CNG SI engine	
Displacement [ℓ]	12.9
Cylinder arrangement	6 in-line vertical
Valves per cylinder	4
Fuel	CNG PFI
Coolant	50% Glycol - 50% Water
Bore x Stroke [mm]	135 × 150
Compression ratio	12
Maximum brake power [kW]	338 @ 1900 rpm
Maximum brake torque [Nm]	2000 @1100/1620 rpm

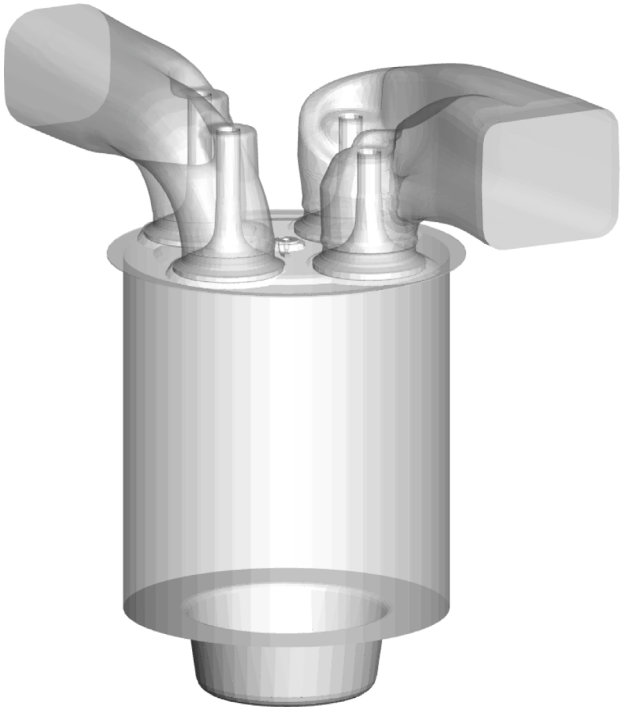

Fig. 3. Cylinder geometry model.

Table 2
Operating condition.

Operating condition	Point 1	Point 2	Point 3	Point 4	Point 5
BMEP [bar]	4.2	3.8	7.5	9.9	19.3
Engine speed [rpm]	1200	1800	1900	800	1400
Spark timing [° CA aTDCf]	−28	−30	−12	−4	−12
Intake mass [g]	1.165	1.125	1.904	2.327	4.391

3.1. Model description

The engine simulations were conducted using CONVERGE CFD 3.0.25, a 3D CFD software that is widely used in the automotive industry [31–35]. The simulations have been performed with a Navier–Stokes density-based solver applying a PISO (Pressure Implicit with Splitting of Operators) scheme, which is particularly effective for transient flow calculations. Turbulence modeling was performed within the RANS framework using the $k-\varepsilon$ RNG model for compressible flow. This model is known for its robustness in handling complex flows with strong streamline curvature and rapid strain, making it suitable for engine simulations. Heat transfer calculations utilized the O'Rourke and Amsden model, complemented by enhanced wall treatment to improve near-wall predictions.

The computational domain was discretized using a base grid of 4 mm, with refinements reaching up to 0.125 mm during combustion

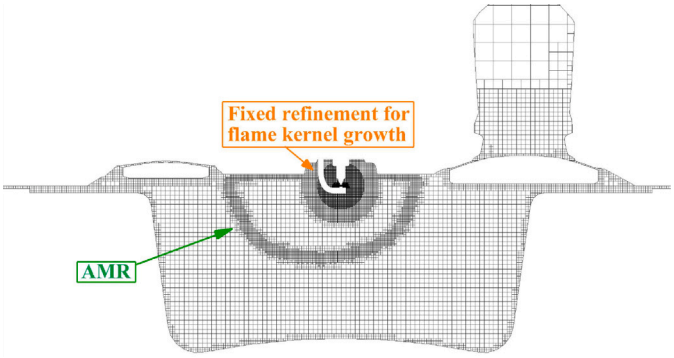

Fig. 4. Mesh near the top dead center firing.

events. This approach, illustrated in Fig. 4, includes fixed embedding boundary layers and cylinder embedding refinement. Additionally, Adaptive Mesh Refinement (AMR) was employed based on velocity and temperature gradients to ensure adequate spatial resolution in regions of interest. For velocity, AMR was applied throughout the entire simulation with a maximum embedding level of 3, and cells were refined when the sub-grid velocity exceeded a threshold of 1 m/s. For temperature, AMR was applied cyclically, starting 30 degrees before top dead center firing and extending to 100 degrees after top dead center firing (aTDCF), with a maximum embedding level of 4 and refinement triggered when the sub-grid temperature exceeded 2.5 K. This strategy resulted in a minimum cell size of 0.25 mm and a maximum of approximately six million cells, maintaining overall computational efficiency. The mesh settings provide sufficient resolution during the compression phase, which is the interval used for the iterative calibration of heat transfer, while the additional refinement during the combustion phase ensures more reliable validation of the updated set of boundary conditions. In particular, in Fig. 4, the effects of AMR during flame front propagation can be clearly appreciated. Time-averaged constant experimental values of intake manifold pressure and temperature are imposed as intake boundary conditions; similarly, the time-averaged experimental exhaust pressure is imposed at the outlet boundary of the exhaust port. Constant space-averaged wall temperature values have been imposed on all the surfaces.

Combustion was simulated using the SAGE solver, which allows for the solution of ODEs to account for chemical kinetics. It must be pointed out that since the proposed methodology focuses on what precedes combustion, no investigations were performed to enhance combustion phase predictions, as well as interaction of chemistry with turbulence. The spark ignition process was modeled with a specified spark discharge power distribution, providing a realistic representation of the ignition event. In order to avoid biases due to initial conditions, the analysis of the numerical results focused on the third cycle for each simulation. Each CFD simulation requires approximately 10 h of wall-clock time on 6 nodes of the CINECA Galileo100 HPC system, with 48 CPU cores per node, corresponding to a total of 288 CPU cores. This results in a computational cost of approximately 2880 core-hours per iteration.

The proposed methodology validation was performed across 5 distinct operating points, which are reported in Table 2. This evaluation on strategic key points ensures the methodology applicability across a wide range of engine operating conditions. The experimental intake mass, used as reference value for the numerical model validation, has been computed by knowing the fuel flow rate and the air-to-fuel ratio. The latter has been determined following the procedure presented in [36], in which the concentrations of HC, CH_4, NO_x, NO, CO_2, COH and O_2 from emission sensors are used to compute air-to-fuel ratio of the mixture with an uncertainty of 1%. As an alternative, a flowmeter could be installed in the intake manifold to directly measure

Table 3
Engine working point 1 iteration results.

Point 1	Preliminary	Iteration 1
m_{int} [g]	1.19	1.163
$E_{\%} m_{int}$ [%]	+2.39	−0.17
$p_{exp,SA}$ [bar]	6.92	6.90
$p_{num,SA}$ [bar]	7.17	6.85
$E_{\%} p_{SA}$ [%]	+3.64	−0.76
$p_{BC,IM}$ [bar]	0.598	0.578
L_w [J]	0.35	0.33
Net Q_{num} [J]	−9.087	−10.583
α [-]	0.957	–
Δ [bar]	0.0344	–

the air mass flow rate. In the presented methodology, the mixture mass per cycle is required, thereby eliminating the need for signal synchronization.

3.2. Optimization results: wall temperatures from a preliminary 1D-CFD model

In this section, the methodology has been applied to the engine points 1, 2, 3 and 4 (point 5 will be analyzed in Section 3.3), and preliminary values of the combustion chamber wall temperatures are those resulting from a previously validated 1D diagnostic model.

These temperatures are valid as a first attempt solution for the boundary conditions, although they are not optimal for the sake of the 3D-CFD simulations. This is evident from the results reported in Table 3, which refer to engine point 1: for the preliminary simulation, the intake mass and the pressure at spark timing show an error of +2.39% and +3.64%, respectively compared to available experimental data. It should be noted that the experimental pressure trace was determined as the average of all the acquired cycles for all the cylinders (100 consecutive cycles were measured for each cylinder): each pressure trace has been filtered before averaging using a lowpass filter with a cutoff frequency of 4 kHz; it should be noted that all curves have been preliminary referenced to the pressure in the intake manifold by imposing it as the average in the $-195 \div -175$ °CA aTDCf range.

The methodology illustrated in Section 2 has been applied, assuming that the change in the work of viscous dissipation L_w due to the pegging is negligible compared to the change in the heat transfer (the consistency of this assumption has been verified for all the working conditions). The integrals in the methodology have been computed from the intake valve closure timing (−175 °CA aTDCf) to the spark timing, which depends on the engine working point as reported in Table 2.

In order to correct the in-cylinder pressure overestimation at the spark timing, the in-cylinder experimental pressure has been pegged by selecting a shift of $\Delta = 3435$ Pa $= 2.418 \cdot \delta$ (when $\Delta > 0$, the pressure signal is shifted downwards, cf. Eq. (13)). From Fig. 5 the effect of pegging on the experimentally-based heat transfer can be appreciated compared with the numerical one.

The h_i coefficients are then computed using the steps described in Section 2.3. With the aim of clarifying how the optimization of h works, in Fig. 6 are shown the trends of the different h considered for the intake valve boundary (cf. Fig. 2). Specifically, the blue curve is the one calculated by Converge from the computation of the heat flux to the walls (cf. Eq. (7)); the green solid line is the application of the definition of heat transfer coefficient (cf. Eq. (8)); finally, with dashed red line the heat transfer coefficient optimized by the procedure is plotted. The ranges of the $h_i(t)$ for engine point 1 are shown in Table 4. The surface-weighted average of the h_i heat transfer coefficients of each boundary, namely, $h = (A_i\ h_i)/\sum A_i$, shows a trend that is comparable to that obtained for the Woschni model [24] for all the investigated engine points. As already mentioned, the h_i represents the convection coefficient for each boundary, computed using the difference between

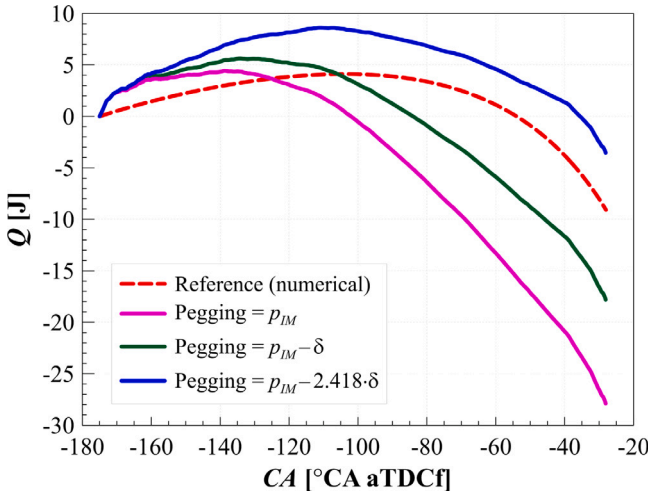

Fig. 5. Comparison between the curves of the numerical heat transfer through the walls and the pegged experimental ones, for different pegging shifts referring to the preliminary simulation of engine working point 1.

Table 4
Ranges of the value of the $h_i(t)$ in [$Wm^{-2}K^{-1}$]. Maximum, minimum and mean values for each boundary (engine point 1).

h_i [$Wm^{-2}K^{-1}$]	Max	Min	Mean
Head	370.9	45.7	175.4
Intake valve	402.1	176.7	111.9
Exhaust valve	424.7	50.8	152.3
Spark	987.2	110.3	249.1
Liner	322.2	101.1	204.9
Piston	500.9	80.5	257.6

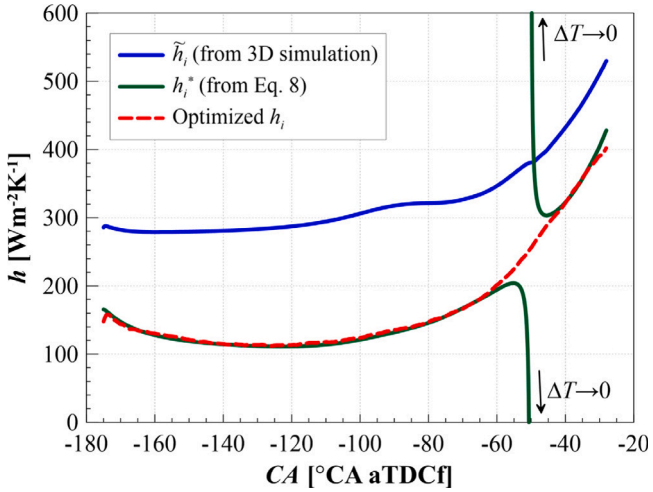

Fig. 6. Comparison between the different h for the intake valve boundary for engine working point 1.

the temperature of each wall and the mean temperature of the gas in the combustion chamber.

For the selected Δ value, the equality between the numerical and the experimentally-based heat transfer during the compression phase depicted in Fig. 5, based on Eq. (6), is achieved by applying a multiplication factor $\alpha = 0.957$ to the combustion chamber wall temperatures, meaning that the values of T_{wall} have been reduced by 4.32%.

Therefore, a new simulation, labeled as Iteration 1, has been performed with the new set of boundary conditions. As can be seen in Table 3, both the simulated pressure at spark timing and the intake

Table 5
Engine working point 2 iteration results.

Point 2	Preliminary	Iter. 1	Iter. 2
m_{int} [g]	1.156	1.138	1.124
$E_{\%}m_{int}$ [%]	+2.76	+1.21	−0.05
$p_{exp,SA}$ [bar]	6.5	6.49	6.49
$p_{num,SA}$ [bar]	6.6	6.53	6.51
$E_{\%}p_{SA}$ [%]	+1.5	+0.66	+0.32
$p_{BC,IM}$ [bar]	0.626	0.619	0.616
L_w [J]	0.51	0.52	0.51
Net Q_{num} [J]	−2.747	−2.782	−0.583
α [-]	1.019	1.037	–
Δ [bar]	0.0513	0.0464	–

mass are consistent with experimental data ($E_{\%}p_{SA} = -0.76\%$ and $E_{\%}m_{int} = -0.17\%$, respectively). Furthermore, the log–log diagrams reported in Figs. 7(a) and 7(b) show that the inaccuracy along the entire compression phase featured in the preliminary simulation improves appreciably the BCs correction. A detail of the difference between experimental and numerical pressure traces of the two iterations is presented in Fig. 7(c). For the corrected simulation, the difference is much smaller during the whole compression phase with respect to the preliminary simulation, which diverged at spark timing.

Therefore, for engine working point 1, a single iteration, with minimal pressure and wall temperature corrections, equal to −3.36% and −4.32%, respectively, enables to converge to an optimal result. For this low-load and low-speed operating point the correction strategy focused primarily on the pressure curve pegging. Since the intake mass was slightly overestimated, the intake pressure value was reduced by acting on Δ in order to reduce the in-cylinder pressure inaccuracy at spark timing ($p_{BC,IM}$ was reduced by 3.34% in the first iteration, while the error at spark-timing passed from +3.64% to −0.76%). The influence of the wall temperatures scaling factor was secondary because the total heat transfer through the wall was relatively small, due to the limited temperature gradients between the in-cylinder gas and the walls. In Table 3 and throughout the remainder of the paper, a positive sign is assigned to heat absorbed by the gas from the walls, while heat released by the gas to the walls is considered negative. The pressure trace during combustion for point 1 is shown in Fig. 8. It is possible to appreciate a good agreement of the numerical result with the expected experimental average pressure, with simulation results satisfactorily inside the cycle-to-cycle variability after the correction is applied.

For the other three engine operating points, namely points 2–4 in Table 2, convergence to an optimal set of boundary conditions was similarly achieved within just 2 or 3 iterations. Table 5 summarizes the key results for engine working point 2, while the final outcome is illustrated in Fig. 9. The first iteration was set imposing a Δ value which resulted in a shift of the intake-manifold pressure boundary condition comparable to the pressure error at spark timing (i.e., the $p_{BC,IM}$ was changed of −1.1% in the first iteration, while the error at spark timing passed from +1.5% to +0.66%), this being in line with the strategy adopted for engine point 1. For engine point 2, the high engine speed leads to a shorter compression duration, further limiting the importance of the heat transfer for this working point.

In Table 6 the results of iterations for engine working point 3 are shown. In this case, 3 iterations were performed because the initially selected value of Δ was not large enough to compensate both the pressure and mass errors primarily with the wall temperatures change. The convergence was easily reached when a relatively larger Δ (+15%) was chosen. The final result can be appreciated in Fig. 10. It could be noticed that the absolute value of the overall shift to the intake manifold pressure boundary condition is in line with the other points. Being a medium-load, high-speed operating point, it is characterized by more pronounced temperature gradients between in-cylinder gas and walls than engine points 1 and 2, although for a short amount of time. As a consequence, the first iteration corrected significantly the

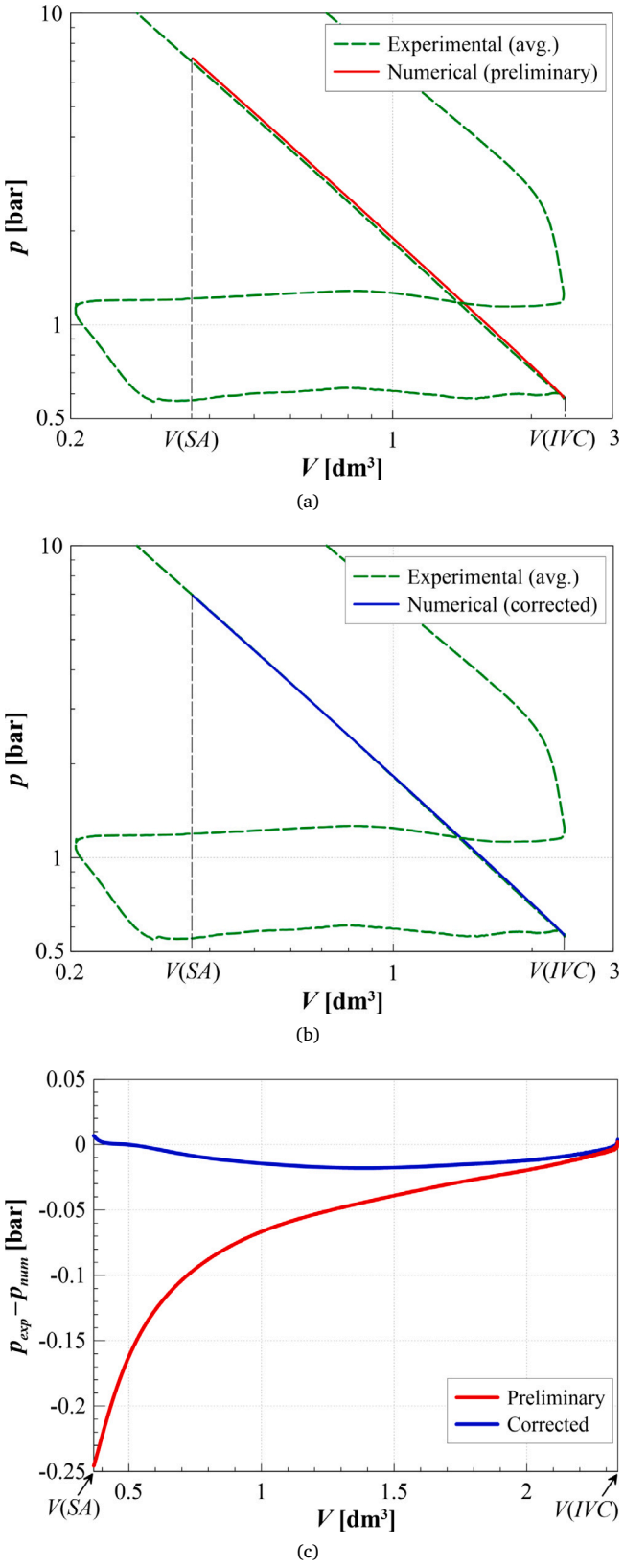

Fig. 7. Comparison between experimental and numerical results during the compression phase curves for engine working point 1: (a) log$p$-log$V$ curves before the correction; (b) log$p$-log$V$ curves after the correction; (c) difference between the experimental and numerical pressure traces before and after the correction.

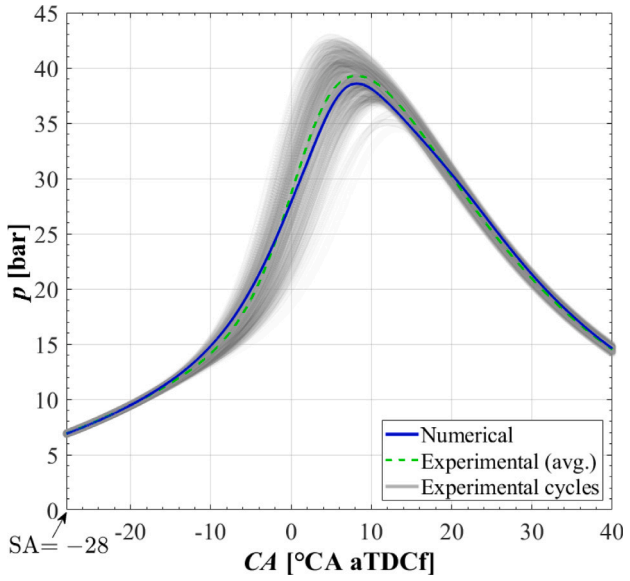

Fig. 8. Comparison between the numerical and experimental curves during combustion for engine working point 1.

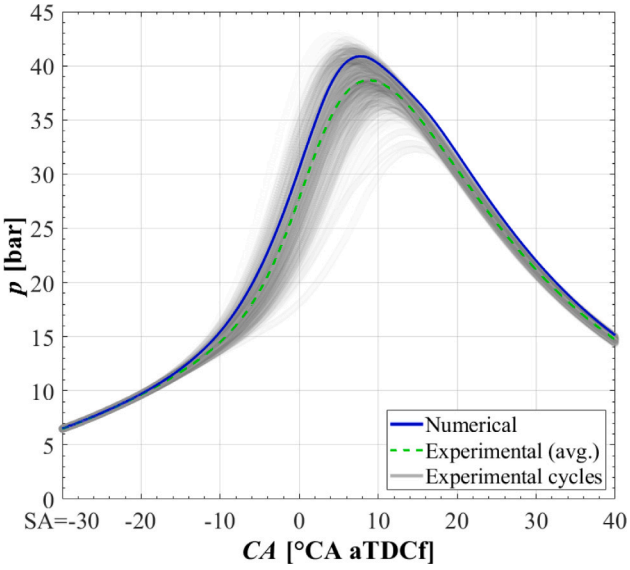

Fig. 9. Comparison between the numerical and experimental curves during combustion for engine working point 2.

wall temperatures through the scaling factor α and a slight reduction of the intake pressure was implemented. All this led to an improvement in the pressure error at spark timing but caused an increment in the intake mass inaccuracy. In the subsequent iterations, the correction strategy relied mainly on adjusting the pressure, selecting Δ in order to achieve $Q_{num} \approx Q_{exp}$ (cf. $\alpha \approx 1$ in Iter. 1 of Table 6). As expected, the final value of the net heat transfer is higher than in the previous two operating points. After two other iterations, convergence was reached to the tolerances set for errors on mass and pressure at spark-timing. The performance of the numerical model in simulating the combustion process is satisfactory since the numerical pressure trace matches the experimental one.

Similar considerations apply to engine working point 4. The results of the iterative process are presented in Table 7, while the final in-cylinder pressure trace during combustion is shown in Fig. 11. For all the considered engine working conditions, L_w variation between

Table 6
Engine working point 3 iteration results.

Point 3	Prelim.	Iter. 1	Iter. 2	Iter. 3
m_{int} [g]	2.01	2.03	2.015	1.974
$E_{\%} m_{int}$ [%]	+5.78	+6.66	+5.86	+3.69
$p_{exp,SA}$ [bar]	21.59	21.58	21.58	21.61
$p_{num,SA}$ [bar]	22.14	21.84	21.81	21.46
$E_{\%} p_{SA}$ [%]	+2.55	+1.23	+1.1	−0.70
$p_{BC,IM}$ [bar]	1.058	1.053	1.048	1.037
L_W [J]	1.31	1.26	1.33	1.30
Net Q_{num} [J]	−18.670	−24.737	−23.380	−19.462
α [-]	0.929	1.014	1.044	–
Δ [bar]	0.0629	0.0681	0.0724	–

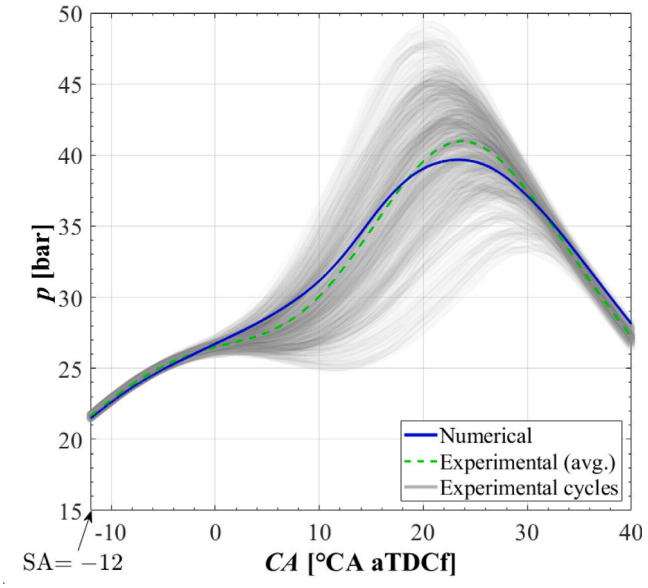

Fig. 10. Comparison between the numerical and experimental curves during combustion for engine working point 3.

Table 7
Engine working point 4 iteration results.

Point 4	Prelim.	Iter. 1	Iter. 2
m_{int} [g]	2.44	2.31	2.28
$E_{\%} m_{int}$ [%]	+4.67	−0.43	−2.02
$p_{exp,SA}$ [bar]	28.25	28.21	28.20
$p_{num,SA}$ [bar]	29.20	28.69	28.36
$E_{\%} p_{SA}$ [%]	+3.37	+1.71	+0.55
$p_{BC,IM}$ [bar]	1.132	1.095	1.089
L_w [J]	0.65	0.75	0.70
Net Q_{num} [J]	−43.728	−21.964	−20.559
α [-]	1.106	1.023	–
Δ [bar]	0.0511	0.0179	–

different iterations is marginal, meaning that the effect of any possible inaccuracies in boundary conditions is negligible for its estimation.

Table 8 reports a summary of the results of the application of the proposed methodology to the considered four engine working points. In particular, the errors on pressure at spark timing and intake mass for the preliminary and final iterations can be compared, besides the overall variations for wall temperatures and intake manifold pressure boundary conditions are reported.

As can be inferred from Table 8, if the pressure at spark timing results to be overestimated in the preliminary simulation, the methodology reduces the intake pressure boundary condition. Furthermore, since the temperatures of the preliminary simulations were provided by a validated 1D engine model, the intake pressure was modified in order to keep α around 1. It can be seen that the resulting total correction

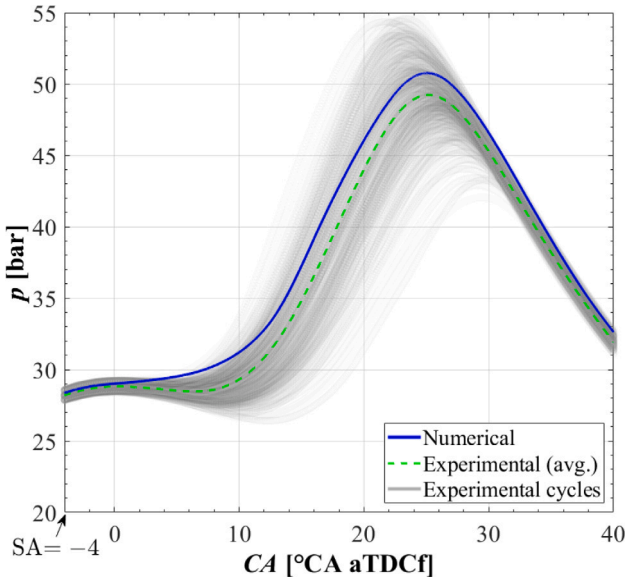

Fig. 11. Comparison between the numerical and experimental curves during combustion for engine working point 4.

Table 8
Summary of pressure at spark-timing and intake mass inaccuracies and boundary condition variations.

	Point 1	Point 2	Point 3	Point 4
Initial $E_{\%}p_{SA}$ [%]	+3.64	+1.57	+2.55	+3.37
Final $E_{\%}p_{SA}$ [%]	−0.76	+0.32	−0.70	+0.55
Initial $E_{\%}m_{int}$ [%]	+2.39	+2.76	+5.78	+4.67
Final $E_{\%}m_{int}$ [%]	+0.09	−0.05	+3.69	−2.02
T_{wall} variation [%]	−4.32	+5.78	+1.57	+13.12
$p_{BC,IM}$ variation [%]	−3.36	−1.62	−1.99	−3.84

of the intake manifold pressure boundary condition is almost equal to percentage value of the initial $E_{\%}p_{SA}$: this leads to a modification of the wall temperatures below 6%, confirming that if the temperatures from a validated 1D model are provided, the source of inaccuracies at the beginning of combustion is mostly due to the intake pressure boundary condition. Engine working point 4 required a higher correction for the wall temperatures: this can be ascribed to a high-load and low-speed engine conditions that both maximize the heat transfer during compression. Furthermore, such an engine working point can be characterized by a more pronounced inaccuracy in the in-cylinder pressure measurement because the compressor is working close to the surge condition (the spread of the experimental pressure curves at spark timing is ±0.4 bar, while it is only of ±0.17 bar for engine working point 3).

If Δ values were slightly different from those selected in the paper, then minor differences would be obtained in the final numerical solutions, in accordance with the well posed problem theory (a physical problem is considered with proper boundary conditions according to the partial differential equations theory).

3.3. Optimization results: absence of data on walls temperatures

Points 1 and 5 from Table 2 have been considered, imposing as tentative boundary conditions the set of generic temperatures shown in Table 9. These temperatures could be representative of a high-load engine point.

Point 1, as previously analyzed, corresponds to a low-load operating condition. As shown in Table 10, the preliminary simulation (Step 0) exhibits a significant overprediction of the in-cylinder pressure at spark timing and an underprediction of the intake mass: such results

Table 9
Generic temperatures for walls BC.

Wall	Temperature [K]
Head	575
Intake valve face	700
Intake valve stem	600
Exhaust valve face	800
Exhaust valve stem	750
Spark plug	775
Liner	450
Piston	550

Table 10
Engine working point 1 iteration results from general temperature boundary conditions.

Point 1, T_{wall} from Table 9	Prelim.	Iter. 1	Iter. 2
m_{int} [g]	1.12	1.19	1.11
$E_{\%}m_{int}$ [%]	−3.61	+2.6	−4.72
$p_{exp,SA}$ [bar]	6.92	6.87	6.89
$p_{num,SA}$ [bar]	7.31	7.15	6.90
$E_{\%}p_{SA}$ [%]	+5.64	+4.16	+0.07
$p_{BC,IM}$ [bar]	0.598	0.598	0.573
L_w [J]	0.35	0.32	0.31
Net Q_{num} [J]	+1.266	−9.245	−3.198
α [-]	0.790	1.058	–
Δ [bar]	0.0095	0.0401	–

are consistent with an engine simulation where the wall temperatures are strongly overestimated, leading to a poor volumetric efficiency and a high pressure at the end of compression, due to an excessive heat transfer from walls to the in-cylinder charge. Therefore, given that the wall temperatures reported in Table 9 are comparable to the boundary conditions typically associated with high-load engine points, the first iteration aimed to substantially reduce these temperatures while maintaining the intake pressure boundary condition.

This adjustment resulted in a temperature scaling factor $\alpha = 0.79$, corresponding to a 21% reduction in wall temperatures. This change led to a notable initial improvement in pressure at spark timing and intake mass, as can be noticed by the results pertaining to Iter. 1 in Table 10.

In accordance with the strategy outlined at the end of Section 3.2, the intake pressure was subsequently reduced by approximately the same percentage as the relative error in pressure at spark timing, $E_{\%}p_{SA}$, corresponding to $\Delta = 0.0401$ bar. The second iteration yielded satisfactory results, confirming the robustness of the proposed methodology, regardless of the combustion chamber wall temperature boundary conditions assumed for the preliminary simulation.

In an effort to reduce the error in the intake mass, the correction factor α for setting a third iteration was computed preserving the intake pressure boundary condition. The resulting adjustment would lead to an increase in wall temperature of less than 1%. Hence, given the negligible impact of such a variation and the computational effort required, no additional iterations, beyond iteration 2, should be considered necessary.

In Fig. 12 the red curve represents the pressure trend obtained from the iteration 2 shown in Table 10, while the blue curve corresponds to the final iteration of Table 3. Both conditions result in numerical pressure curves closely matching the average experimental pressure, particularly around combustion onset, where errors on pressure remain minimal. Temperature boundary conditions are respectively T_{head} = 511.3 K, T_{piston} = 489.06 K, T_{liner} = 400.14 K for the red curve, i.e., the final iteration of Table 10 and T_{head} = 444.22 K, T_{piston} = 419.11 K and T_{liner} = 373.56 K for the blue curve, i.e., the final iteration of Table 3. Notably, the different temperatures found influence the derivative of the pressure during combustion, as reported in [7]. The existence of more than one distinct yet acceptable solutions can be attributed to the inherent approximation in the boundary condition formulation, where

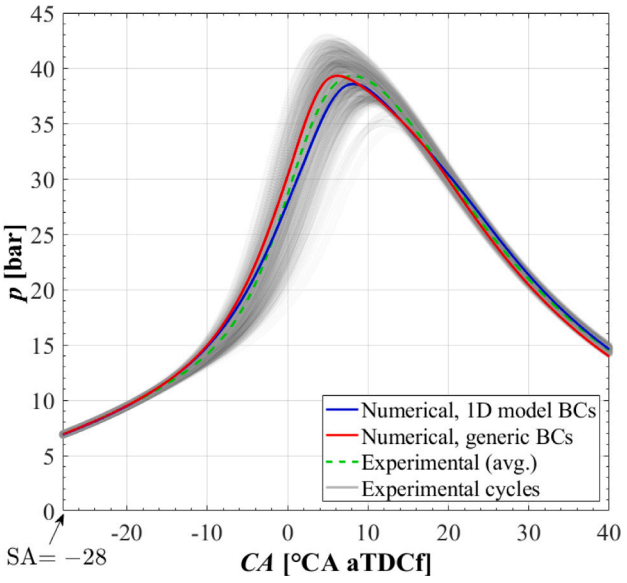

Fig. 12. Comparison of numerical results for engine working point 1 with 1D model BCs and general BCs.

wall temperatures are assumed to be spatially and temporally constant. This simplification, while commonly adopted, inevitably introduces uncertainty. A limitation of the presented methodology is the fixed temperature ratio across boundaries, which enables the definition of only a single global scaling coefficient α across all boundaries, which is valid when the engine has reached a steady-state thermal regime. While this approach reduces computational complexity, it constrains the model flexibility in capturing localized thermal effects. As a potential improvement, introducing additional equations to independently adjust the wall temperatures could enhance the accuracy of the combustion evolution, allowing for a more realistic representation of temperature boundary conditions. Nevertheless, the computational efficiency gained by this simplified approach justifies its use, and to demonstrate the reliability of this methodology, an additional simulation to test convergence of the proposed methodology has been performed on engine working point 1. The ratios between the wall temperatures were fixed according to the validated 1D model as in Section 3.2, and such temperatures were arbitrarily multiplied times 1.2385 to have T_{head} = 575 K. Using the same iterative approach as for the general temperature case (cf. Table 10), convergence was again achieved, with intake manifold pressure and wall temperatures almost coincident with those reported in Table 3 for Iteration 1. The results can be found in Table 11. As an example, after iteration 1, one obtains T_{head} = 445.7 K: together with an intake pressure of 0.578 bar, this corresponds to almost the same set of boundary conditions as those achieved in Iteration 1 and reported in Table 3 (where T_{head} = 444.22 K and $p_{BC,IM}$=0.578 bar). For this reason, iteration 2 in Table 11 was not performed, since the numerical result would be almost coincident with that reported in Fig. 8. This demonstrates that, once the ratio of wall temperatures is fixed, the methodology consistently converges to a unique set of boundary conditions. The small differences observed in wall temperature values between Iteration 1 in Table 3 and Iteration 2 in Table 11, are consistent with the existence of an admissible tolerance in the presented procedure.

Finally, engine working point 5 is a high-load point, therefore the temperatures reported in Table 9 are already a fair preliminary hypotesis: indeed, the temperatures resulting from the validated 1D model would not be much different. As a consequence, a single iteration has been sufficient to converge within the threshold errors for pressure at spark timing and intake mass (cf. Table 12).

Table 11
Engine working point 1 iteration results from increased temperatures from 1D model.

Point 1, scaled T_{wall} from 1D model	Preliminary	Iter. 1	Iter. 2
m_{int} [g]	1.11	1.20	–
$E_{\%} m_{int}$ [%]	−4.58	3.25	–
$p_{exp,SA}$ [bar]	6.90	6.87	–
$p_{num,SA}$ [bar]	7.32	7.13	–
$E_{\%} p_{SA}$ [%]	+6.10	3.77	–
$p_{BC,IM}$ [bar]	0.598	0.598	0.578
L_w [J]	0.37	0.32	–
Net Q_{num} [J]	+1.382	−11.286	–
α [-]	0.73	0.99	–
Δ [bar]	0.0086	0.0356	–

Table 12
Engine working point 5 iteration results from general temperature boundary conditions.

Point 5, T_{wall} from Table 9	Prelim.	Iter. 1
m_{int} [g]	4.86	4.51
$E_{\%} m_{int}$ [%]	+6.18	−1.58
$p_{exp,SA}$ [bar]	55.14	55.00
$p_{num,SA}$ [bar]	59.06	55.45
$E_{\%} p_{SA}$ [%]	+7.10	+0.81
$p_{BC,IM}$ [bar]	2.329	2.180
L_w [J]	1.12	1.08
Net Q_{num} [J]	+1.412	+16.504
α [-]	1.033	–
Δ [bar]	0.0199	–

The methodology therefore demonstrates convergence in no more than three iterations, regardless of engine load and speed. For comparison purposes, a fully factorial DoE would typically require about 1800 full 3D CFD simulations (steps of 5 mbar to cover a range of 0.3 bar have been considered for $p_{BC,IM}$ and steps of 0.015 to cover a range of 0.4 have been considered for the dimensionless factor α) with an unacceptable computational cost. The application of strategies to reduce the computational cost of the DoE could not overperform the proposed iterative procedure, which converged within 3 CFD runs for the analyzed working conditions.

4. Conclusion

The paper presented a novel methodology for optimizing the boundary conditions of combustion chamber wall temperatures and intake pressure in 3D-CFD simulations of internal combustion engines. This approach, grounded in the laws of thermodynamics, leverages a multi-zone wall heat transfer model in conjunction with 3D-CFD RANS simulations, resulting to be both engine-type and fuel independent provided that mass exchange through the combustion chamber walls is negligible (only leakages can exist) during the compression stroke and the heat transfer is mainly convective. These assumptions, hence, in principle could exclude the application of this methodology to direct injection engines with carbon-based fuels (because soot formation adds radiation) or with early injection during the compression stroke. The iterative application of the methodology enables more accurate predictions of the in-cylinder pressure at spark timing and the intake mass in the cylinder, reducing the number of required simulations and thus the overall computational time needed for 3D-CFD model calibration. The methodology was validated across five different engine points of a spark-ignited heavy-duty PFI engine fueled with CNG. In this context, the methodology is intended not only as a modeling improvement, but also as a practical tool to streamline the calibration workflow of 3D-CFD engine simulations as a systematic alternative to manual or trial-and-error tuning of wall temperature and intake pressure boundary conditions. Notably, when applied to a 3D-CFD numerical model, with wall-temperature boundary conditions derived from a validated

1D diagnostic tool, the methodology improves the accuracy with only minor correction to T_{wall}, and intake pressure corrections proportional to the initial percentage error in pressure prediction at spark timing. Further validations of the wall temperature values or of the wall temperature ratios could be performed according to experimental NO_x emissions, knock tendency or other temperature-sensitive outputs: this could be the scope of a future work.

It has been proved that the methodology is capable to successfully optimize a set of initial wall temperatures that were not provided by a 1D model. In particular, a set of wall temperatures suitable for a high-load point have been applied to a low-load engine point: the methodology allows a substantial reduction of the wall temperature, together with an improvement in the intake pressure boundary condition, leading to an enhanced accuracy of the numerical model. Finally, when a high-load engine point is simulated with such a set of standard temperature for a high-load condition, the methodology allows to reach an accurate prediction in pressure at spark timing and intake mass with a small modification of T_{wall}: this suggests that with the proposed approach it is possible to reduce or even eliminate the need for dedicated 1D diagnostic tools to estimate non-measurable boundary conditions, thus streamlining the 3D-CFD model calibration process.

Declaration of competing interest

The authors declare the following financial interests/personal relationships which may be considered as potential competing interests: Oscar Vento reports financial support was provided by the Italian Ministry of University and Research. Oscar Vento reports financial support was provided by FPT. If there are other authors, they declare that they have no known competing financial interests or personal relationships that could have appeared to influence the work reported in this paper.

Acknowledgments

This study was carried out within the Ministerial Decree no. 1062/2021 and received the fund FSE REACT-EU - PON Ricerca e Innovazione 2014–2020 from Italian Ministry of University and Research. This manuscript reflects only the authors' views and opinions, neither the European Union nor the European Commission can be considered responsible for them. The authors acknowledge CINECA for granting access to the Galileo100 (G100) Tier-1 system. Additional computational resources were provided by HPC@POLITO, a project of academic computing within the Department of Control and Computer Engineering at the Politecnico di Torino (http://www.hpc.polito.it). Both HPCs were instrumental in our computations.

Data availability

The authors do not have permission to share data.

References

[1] Y.-H. Pu, Q. Dejaegere, M. Svensson, S. Verhelst, Renewable methanol as a fuel for heavy-duty engines: a review of technologies enabling single-fuel solutions, Energies 17 (7) (2024) 1719, http://dx.doi.org/10.3390/en17071719.

[2] P.D. Larson, R.V. Parsons, D. Kalluri, Zero-emission heavy-duty, long-haul trucking: Obstacles and opportunities for logistics in North America, Logistics 8 (3) (2024) 64, http://dx.doi.org/10.3390/logistics8030064.

[3] L. Kistner, A. Bensmann, R. Hanke-Rauschenbach, Potentials and limitations of battery-electric container ship propulsion systems, Energy Convers. Manag.: X 21 (2024) 100507, http://dx.doi.org/10.1016/j.ecmx.2023.100507.

[4] Z. Lyu, D. Pons, Y. Zhang, Emissions and total cost of ownership for diesel and battery electric freight pickup and delivery trucks in New Zealand: implications for transition, Sustainability 15 (10) (2023) 7902, http://dx.doi.org/10.3390/su15107902.

[5] S. Safarian, Environmental and energy impacts of battery electric and conventional vehicles: A study in Sweden under recycling scenarios, Fuel Commun. 14 (2023) 100083, http://dx.doi.org/10.1016/j.jfueco.2022.100083.

[6] M. El-Adawy, M.A. Nemitallah, A. Abdelhafez, Towards sustainable hydrogen and ammonia internal combustion engines: Challenges and opportunities, Fuel 364 (2024) 131090, http://dx.doi.org/10.1016/j.fuel.2024.131090.

[7] G. Decan, S. Broekaert, T. Lucchini, G. D'Errico, J. Vierendeels, S. Verhelst, Evaluation of Wall Heat Flux Models for Full Cycle CFD Simulation of Internal Combustion Engines Under Motoring Operation, Tech. Rep., SAE Technical Paper, 2017, http://dx.doi.org/10.4271/2017-24-0032.

[8] L. Fonseca, P. Olmeda, R. Novella, R.M. Valle, Internal combustion engine heat transfer and wall temperature modeling: an overview, Arch. Comput. Methods Eng. 27 (5) (2020) 1661–1679, http://dx.doi.org/10.1007/s11831-019-09361-9.

[9] S. Bürkle, L. Biondo, C.-P. Ding, R. Honza, V. Ebert, B. Böhm, S. Wagner, In-cylinder temperature measurements in a motored IC engine using TDLAS, Flow Turbul. Combust. 101 (2018) 139–159, http://dx.doi.org/10.1007/s10494-017-9886-y.

[10] S. Esposito, M. Mally, L. Cai, H. Pitsch, S. Pischinger, Validation of a RANS 3D-CFD gaseous emission model with space-, species-, and cycle-resolved measurements from an SI DI engine, Energies 13 (17) (2020) 4287, http://dx.doi.org/10.3390/en13174287.

[11] F. Ramognino, L. Sforza, T. Cerri, T. Lucchini, A. Onorati, R. Novella, A Fast and Reliable CFD Approach to Design Hydrogen SI Engines for Industrial Applications, Tech. Rep., SAE Technical Paper, 2023, http://dx.doi.org/10.4271/2023-01-1208.

[12] A. Torregrosa, P. Olmeda, B. Degraeuwe, M. Reyes, A concise wall temperature model for DI diesel engines, Appl. Therm. Eng. 26 (11–12) (2006) 1320–1327, http://dx.doi.org/10.1016/j.applthermaleng.2005.10.021.

[13] Y. Li, S.-C. Kong, Coupling conjugate heat transfer with in-cylinder combustion modeling for engine simulation, Int. J. Heat Mass Transfer 54 (11–12) (2011) 2467–2478, http://dx.doi.org/10.1016/j.ijheatmasstransfer.2011.02.015.

[14] S. Moser, K.D. Edwards, T. Schoeffler, Z.S. Filipi, CFD/FEA co-simulation framework for analysis of the thermal barrier coating design and its impact on the HD diesel engine performance, Energies 14 (2021) 2044.

[15] R. Motwani, J.H. Gandolfo, B. Gainey, A. Levi, S. Moser, Z.S. Filipi, B. Lawler, Assessing the impact of a novel TBC material on heat transfer in a spark ignition engine through 3D CFD-FEA co-simulation routine, SAE Tech. Pap. Ser. (2022).

[16] M. Sideri, A. Berton, F. D'Orrico, Assessment of the wall heat transfer in 3D-CFD in-cylinder simulations of high performance diesel engines, Energy Procedia 126 (2017) 963–970, http://dx.doi.org/10.1016/j.egypro.2017.08.187, ATI 2017 - 72nd Conference of the Italian Thermal Machines Engineering Association.

[17] G. Cicalese, F. Berni, S. Fontanesi, Integrated in-cylinder / CHT methodology for the simulation of the engine thermal field: An application to high performance turbocharged disi engines, SAE Int. J. Engines 9 (2016) 601–617.

[18] C. Sun, B. Deng, J. Yang, R. Feng, C. Chen, A multi-time scales semi-decoupled CHT (coupled heat transfer) model and its application on piston transient heat transfer simulation, Appl. Therm. Eng. 229 (2023) 120548, http://dx.doi.org/10.1016/j.applthermaleng.2023.120548.

[19] P. Holz, T. Bohlke, T. Kramer, CFD–CHT calculation method using buckingham pi-theorem for complex fluid–solid heat transfer problems with scattering boundary conditions, Automot. Engine Technol. 3 (2018) 45–60.

[20] A. Beyer, D. Di Domenico, C. Beatrice, A.C. Kulzer, High-pressure direct injection as enabling technology for high-power density hydrogen SI engines: Experimental analysis of the influence of jet-guided combustion regimes on efficiency and abnormal combustion, Energy Convers. Manage. 326 (2025) 119497, http://dx.doi.org/10.1016/j.enconman.2025.119497, URL https://www.sciencedirect.com/science/article/pii/S0196890425000202.

[21] K. Lee, M. Yoon, M. Sunwoo, A study on pegging methods for noisy cylinder pressure signal, Control Eng. Pract. 16 (8) (2008) 922–929, http://dx.doi.org/10.1016/j.conengprac.2007.10.007, Special Section: IFAC Conference on Analysis and Design of Hybrid Systems (ADHS'06), URL https://www.sciencedirect.com/science/article/pii/S096706610700189X.

[22] G. Borman, K. Nishiwaki, Internal-combustion engine heat transfer, Prog. Energy Combust. Sci. 13 (1) (1987) 1–46, http://dx.doi.org/10.1016/0360-1285(87)90005-0.

[23] Thermodynamics and Fluid Mechanics Group and Annand, WJD, Heat transfer in the cylinders of reciprocating internal combustion engines, Proc. Inst. Mech. Eng. 177 (1) (1963) 973–996.

[24] G. Woschni, A Universally Applicable Equation for the Instantaneous Heat Transfer Coefficient in the Internal Combustion Engine, Tech. Rep., SAE Technical paper, 1967.

[25] S. Kirkpatrick, C.D. Gelatt, M.P. Vecchi, Optimization by simulated annealing, Science 220 (4598) (1983) 671–680, http://dx.doi.org/10.1126/science.220.4598.671.

[26] B. Wang, J. Xu, B. Cao, B. Ning, Adaptive mode switch strategy based on simulated annealing optimization of a multi-mode hybrid energy storage system for electric vehicles, Appl. Energy 194 (2017) 596–608, http://dx.doi.org/10.1016/j.apenergy.2016.05.030.

[27] R. Zou, B. Wang, K. Wang, W.-L. Shang, D. Xue, W.Y. Ochieng, A pathway to sustainable aviation: Modeling aircraft takeoff mass for precise fuel consumption and aircraft emission calculations, Energy 319 (2025) 135074, http://dx.doi.org/10.1016/j.energy.2025.135074.

[28] Y. Cui, H. Xu, F. Zou, Z. Chen, K. Gong, Optimization based method to develop representative driving cycle for real-world fuel consumption estimation, Energy 235 (2021) 121434, http://dx.doi.org/10.1016/j.energy.2021.121434.

[29] M. Liu, Y. Shi, J. Yan, Y. Yan, Lattice Boltzmann simulation of flow and heat transfer in random porous media constructed by simulated annealing algorithm, Appl. Therm. Eng. 115 (2017) 1348–1356, http://dx.doi.org/10.1016/j.applthermaleng.2016.12.107.

[30] F.A. Potra, S.J. Wright, Interior-point methods, J. Comput. Appl. Math. 124 (1) (2000) 281–302, http://dx.doi.org/10.1016/S0377-0427(00)00433-7, Numerical Analysis 2000. Vol. IV: Optimization and Nonlinear Equations.

[31] Y. Li, H. Li, H. Guo, Y. Li, M. Yao, A numerical investigation on methane combustion and emissions from a natural gas-diesel dual fuel engine using CFD model, Appl. Energy 205 (2017) 153–162, http://dx.doi.org/10.1016/j.apenergy.2017.07.071.

[32] Z. Zhang, S. Wang, M. Pan, J. Lv, K. Lu, Y. Ye, D. Tan, Utilization of hydrogen-diesel blends for the improvements of a dual-fuel engine based on the improved taguchi methodology, Energy 292 (2024) 130474, http://dx.doi.org/10.1016/j.energy.2024.130474.

[33] J. Shu, J. Fu, J. Liu, Y. Ma, S. Wang, B. Deng, D. Zeng, Effects of injector spray angle on combustion and emissions characteristics of a natural gas (NG)-diesel dual fuel engine based on CFD coupled with reduced chemical kinetic model, Appl. Energy 233 (2019) 182–195, http://dx.doi.org/10.1016/j.apenergy.2018.10.040.

[34] Z. Zhang, S. Wang, M. Pan, J. Lv, K. Lu, Y. Ye, D. Tan, Utilization of hydrogen-diesel blends for the improvements of a dual-fuel engine based on the improved taguchi methodology, Energy 292 (2024) 130474, http://dx.doi.org/10.1016/j.energy.2024.130661.

[35] Z. Lian, W. Li, Y. Cai, H. Chen, J. Jiang, G. Li, F. Zhao, W. Yu, Investigations of diesel and natural gas injection interaction on combustion characteristics of a high-pressure direct-injection dual-fuel engine based on large eddy simulation, Appl. Energy 378 (2025) 124807, http://dx.doi.org/10.1016/j.apenergy.2024.124807.

[36] S. d'Ambrosio, R. Finesso, E. Spessa, Calculation of mass emissions, oxygen mass fraction and thermal capacity of the inducted charge in SI and diesel engines from exhaust and intake gas analysis, Fuel 90 (1) (2011) 152–166, http://dx.doi.org/10.1016/j.fuel.2010.08.025.